

Hypernet-Ensemble Learning of Segmentation Probability for Medical Image Segmentation with Ambiguous Labels

Sungmin Hong
MGH, HMS

Anna Bonkhoff
MGH, HMS

Andrew Hoopes
MGH, HMS

Martin Bretzner
MGH, HMS

Markus Schirmer
MGH, HMS

Anne-Katrin Giese
UKE

Adrian Dalca
MGH, HMS & MIT

Polina Golland
MIT CSAIL

Natalia Rost
MGH, HMS

Abstract

Despite the superior performance of Deep Learning (DL) on numerous segmentation tasks, the DL-based approaches are notoriously overconfident about their prediction with highly polarized label probability. This is often not desirable for many applications with the inherent label ambiguity even in human annotations. This challenge has been addressed by leveraging multiple annotations per image and the segmentation uncertainty. However, multiple per-image annotations are often not available in a real-world application and the uncertainty does not provide full control on segmentation results to users. In this paper, we propose novel methods to improve the segmentation probability estimation without sacrificing performance in a real-world scenario that we have only one ambiguous annotation per image. We marginalize the estimated segmentation probability maps of networks that are encouraged to under-/over-segment with the varying Tversky loss without penalizing balanced segmentation. Moreover, we propose a unified hypernetwork ensemble method to alleviate the computational burden of training multiple networks. Our approaches successfully estimated the segmentation probability maps that reflected the underlying structures and provided the intuitive control on segmentation for the challenging 3D medical image segmentation. Although the main focus of our proposed methods is not to improve the binary segmentation performance, our approaches marginally outperformed the state-of-the-arts. The codes are available at <https://github.com/sh4174/HypernetEnsemble>.

1. Introduction

Deep learning (DL) based methods have been the prime choices for image segmentation tasks in the past decade [38, 47, 53, 62]. Despite their superior performance, DL networks are notoriously overconfident about their predictions that the estimated probabilities of the predicted segmenta-

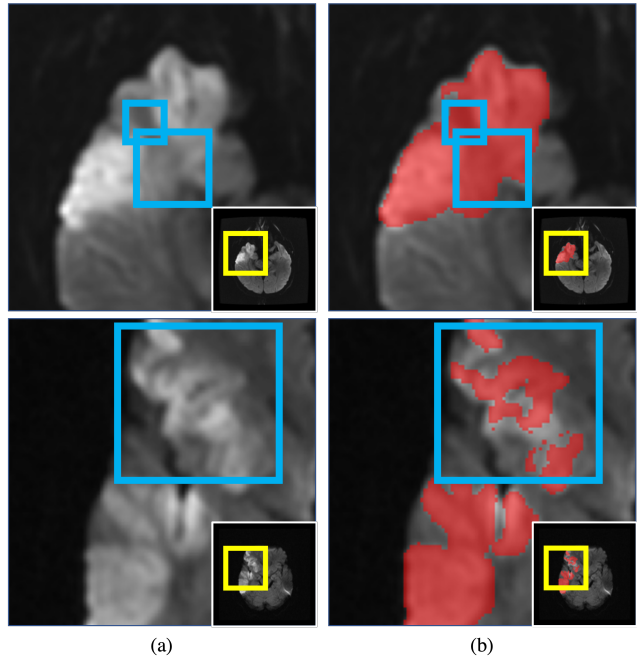


Figure 1. Human annotations on ambiguous stroke lesions. Ambiguous areas (blue squares) in the top and bottom rows caused by the same pathological variability and the partial volume effect were annotated differently. The images are sliced and zoomed from 3D images shown in the right-bottom corners for visibility.

tion labels are polarized close to zero or one [33, 39, 48, 53].

In many applications, especially in medicine, the polarized segmentation probability is often not desirable because there are many factors that cause the inherent ambiguity in annotations even for experienced human experts, e.g., the partial-volume effect, the continuous lesion infarction process, or annotator fatigue [2, 6, 11, 33, 42, 56, 59, 65]. Fig. 1 (b) shows the examples of the human annotations of ambiguous stroke lesions in two diffusion weighted images (DWIs, Fig. 1 (a)) [14]. Ambiguous lesion areas (blue squares) caused by the lesion diffusion in the image at the

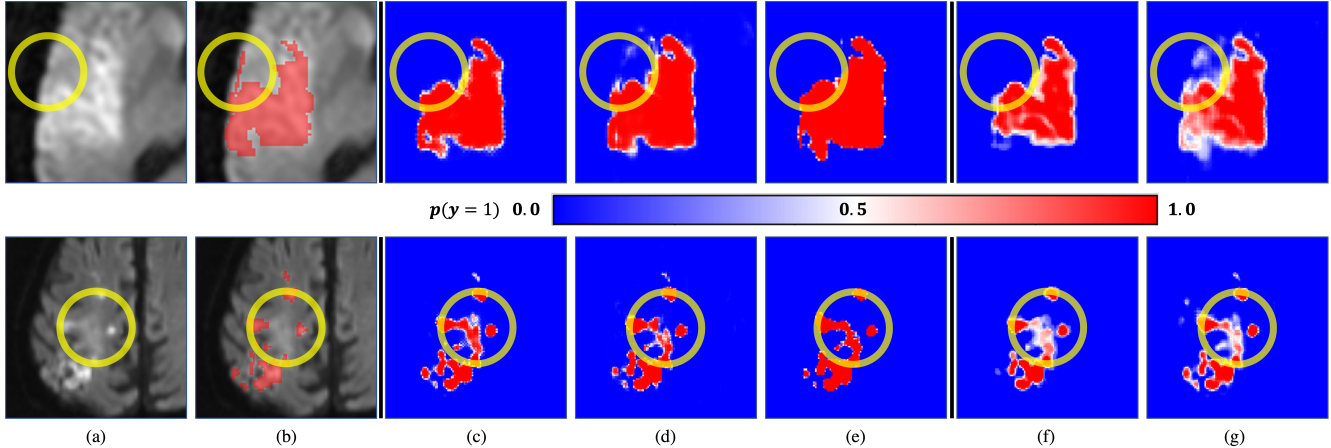


Figure 2. The comparisons of the estimated segmentation probability maps. (a) input images, (b) human annotations, (c) ResUNet, (d) UNETR, (e) UNETR ensembles with different data subsets, (f) UNETR ensembles with the varying Tversky loss (ours), and (g) Hypernetwork ensembles with varying Tversky loss (ours). The ambiguous areas caused by image artifacts (yellow circle, top row) and different pathology (yellow circle, bottom row) were both estimated to have 0.5 probability by the proposed methods(f-g).

top row were annotated by a human expert while not annotated in another image at the bottom row.

Many approaches were proposed to overcome this challenge by leveraging the segmentation uncertainty and multiple annotations per image. The network ensemble approaches that ensemble the outputs of multiple DL networks trained by different configurations [7, 12, 13, 16, 19, 35, 40, 41, 61, 69, 71] and implicit ensemble approaches [12, 21, 60] were proposed to improve the generalization of the DL networks. However, their uncertainty maps did not fully represent the underlying structures of objects. Another popular choice is the M-heads method that estimates multiple label candidates [22, 36, 55]. The stochastic networks are also popular choices to model the uncertainty and generate multiple label candidates [3, 26, 32, 48, 56]. However, the methods often rely on multiple annotations per image and do not directly offer a segmentation probability map that can provide an intuitive control to users to adjust the estimated segmentation label maps.

In this paper, we aim to improve the segmentation probability estimation for medical image segmentation in a common real-world scenario that we only have one ambiguous annotation per each image without sacrificing the performance of the DL networks on the binary segmentation. We choose to model segmentation probability maps directly rather than modeling the uncertainty to provide intuitive control on different segmentation results to end-users.

Our hypothesis is that we can estimate the underlying segmentation probability map by marginalizing the segmentation label maps estimated by networks that are encouraged to under-/over-segment while not penalizing the balanced segmentation. We first propose the network ensemble approach that leverages the varying Tversky loss [57]. The Tversky loss was first suggested for medical image

segmentation to tackle the imbalanced segmentation problem [57]. We leverage the flexibility of the Tversky loss that can encourage the network to under-/over-segment without penalizing the balanced segmentation by varying its hyperparameters. To overcome the high computational requirement of the proposed network ensemble approach, we also propose a unified approach leveraging a hypernetwork architecture [15, 20] that learns different configurations of the primary network with respect to the hyperparameter of the varying Tversky loss. We show the feasibility and strength of our proposed methods and compare them to the state-of-the-arts on 3D medical images in application to the acute stroke lesion segmentation with clinical-grade DWIs collected from multiple hospitals [14].

Our contributions can be largely summarized as follows: 1) We improve the segmentation probability map (shown in Fig. 2) estimation to reflect underlying structures from a single ambiguous annotation per image without sacrificing the binary segmentation performance. 2) It is the first attempt in our knowledge to leverage the combinations of the network and hypernetwork ensemble approaches with varying Tversky loss to improve the segmentation probability estimation. 3) The propose methods offer an intuitive control on the binary segmentation results by simply choosing different probability thresholds.

1.1. Related works

In this subsection, we will summarize the previous works that our proposed methods are built upon.

Medical Image Segmentation There are a plethora of papers on medical image segmentation as it is a fundamental task in medicine to delineate anatomical structures [10, 52, 58]. Since the UNet [53], the DL-based approaches have become the standard in medical image segmentation

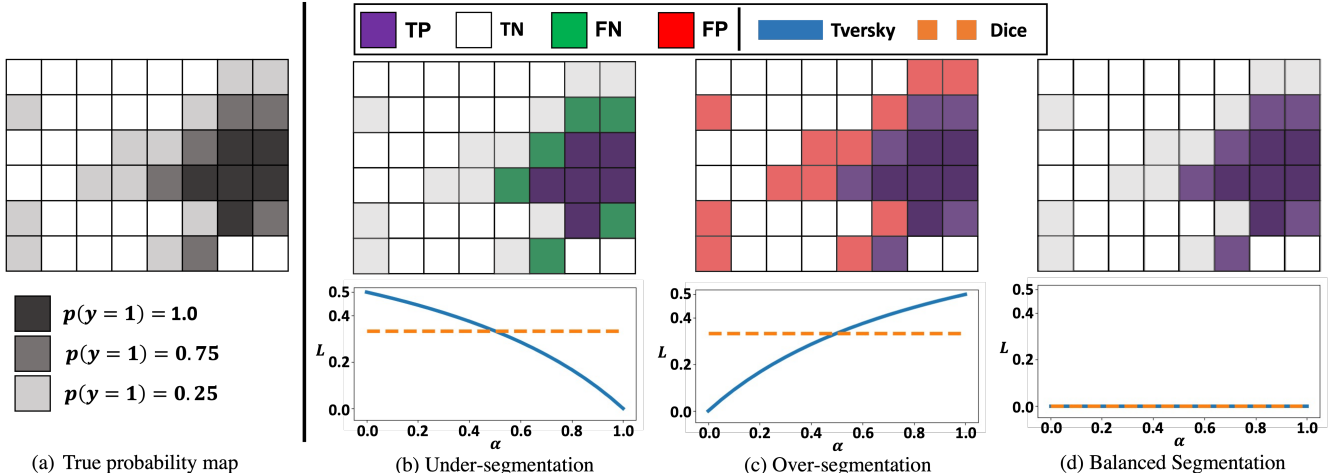


Figure 3. (Top) The illustrations of under- and over-segmentation with the hypothetical *true* probability map with true positive (TP, purple), true negative (TN, white), false negative (FN, green), and false positive (FP, red) labels. (Bottom) The corresponding Tversky loss L with varying hyperparameter α . The undersegmentation is less penalized with higher α while the oversegmentation is less penalized with lower α . The balanced segmentation is always encouraged regardless the choice of α .

and shown successful results [24, 50, 58]. Because the data imbalance and the label ambiguity, many approaches were suggested to manipulate loss functions to achieve better performance, e.g., the Tversky loss [1, 4, 43, 57]. Recently, the multi-head transformer-based approach showed the state-of-the-art performance with 3D brain images [17].

Hypernetworks The hypernetwork architecture was suggested in [15] to mitigate the computational burden of DL networks by estimating the weights of a primary network. It was applied to many applications including image recognition, neural architectural search and neural representations [15, 23, 31, 44, 49, 68]. The hypernetwork was used in medical applications to alleviate the computational burden of the hyperparameter search for image registration and reconstruction [20, 67]. It was also applied to real-time semantic segmentation and medical image segmentation and showed successful results [45, 49].

Network Ensembles The network ensemble is a popular approach to improve the generalization of DL networks [12, 16, 35, 71]. Typically, the network ensemble approaches include: 1) the k -fold cross-validation strategy that trains multiple networks with different subsets of training data and random initialization of the networks [35, 40, 61], 2) different network/training configurations [7, 13, 19, 41, 69, 71], and 3) *implicit* ensemble with dropout-like schemes [12, 21, 60]. The reasoning behind employing the network ensemble is that DL networks are easy to converge to local minima because of the large number of parameters. The previous approaches rely on the stochastic characteristics of initialization and data selection in different network training configurations while an individual network is trained on the same objective to achieve the best performance on a given task that may not be optimal for the probability estimation.

2. Varying Tversky Loss

Let us assume that we have an underlying *true* segmentation probability map as illustrated in Fig. 3 (a) from many human experts for binary segmentation. With the *true* probability map, the binary segmentation can be done by simple thresholding. It can be simply formulated as follows,

$$\mathbf{P} = \delta(p(\mathbf{y}), \tau), \quad (1)$$

where $\mathbf{P} \in \{0, 1\}^{W \times H \times D}$ is a predicted segmentation label and $p(\mathbf{y})$ is the *true* probability map of the potential segmentation labels $\mathbf{y} \in \{0, 1\}^{W \times H \times D}$ for a 3D image with the height H , width W , and depth D . δ is the thresholding function with a threshold τ . Low τ will lead to undersegmentation as shown in the top row of Fig. 3 (b), and high τ to oversegmentation as shown in the top row of Fig. 3 (c). Our intuition behind our approach is simple. Since we do not have the *true* probability map and DL networks tend to estimate the highly polarized segmentation probability, we *flip* the problem in Eq. 1 to estimate the segmentation probability map by marginalizing predicted segmentation probability maps from multiple networks encouraged to under-/over-segment while not penalizing balanced segmentation (Fig. 3 (d)). It can be formally stated as follows,

$$p(\mathbf{y}) = \int p(\mathbf{y}; \boldsymbol{\theta} | \mathbf{h}) p(\mathbf{h}) d\mathbf{h}, \quad (2)$$

where \mathbf{h} is a hyperparameter to enforce a network to estimate under-/over-segmentation and $p(\mathbf{y}; \boldsymbol{\theta} | \mathbf{h})$ is the polarized probability maps estimated by a network $\boldsymbol{\theta}$ conditioned on \mathbf{h} . For simplicity, we assume that $\boldsymbol{\theta}$ is determined by \mathbf{h} without stochasticity. One necessary property of $\boldsymbol{\theta} | \mathbf{h}$ is that

it should not penalize the balanced segmentation to guarantee training stability. Otherwise, it may induce undesired extra ambiguity to the segmentation probability estimation.

We leverage the Tversky loss function that scales the effects of false positives (FP) and false negatives (FN) in total loss [57]. The Tversky index S_{Tv} is formulated as follows,

$$S_{Tv}(\mathbf{P}, \mathbf{G}; \alpha, \beta) = \frac{\mathbf{P} \cap \mathbf{G}}{\mathbf{P} \cap \mathbf{G} + \alpha \mathbf{P} \setminus \mathbf{G} + \beta \mathbf{G} \setminus \mathbf{P}}, \quad (3)$$

where \mathbf{P} and \mathbf{G} are a predicted label and a ground truth, respectively. It has two hyperparameters, α and β , controlling the effects of FP, $\mathbf{P} \setminus \mathbf{G}$, and FN, $\mathbf{G} \setminus \mathbf{P}$, respectively [57,66]. When $\alpha=0.5$ and $\beta=0.5$, the S_{Tv} becomes the Dice index S_{Dice} that the effects of FP and FN are equally considered [9,57]. S_{Tv} is used as a loss function for image segmentation similar to the soft Dice loss [57],

$$L_{Tv}(\mathbf{P}, \mathbf{G}; \alpha, \beta) = 1 - S_{Tv}(\mathbf{P}, \mathbf{G}; \alpha, \beta). \quad (4)$$

We focus on the flexibility of the Tversky index $S_{Tv}(\mathbf{P}, \mathbf{G}; \alpha, \beta)$ that can enforce a network to learn to under-/over-segment rather than finding the optimal values of α and β . We constrain α and β to be $0 \leq \alpha \leq 1, \beta = 1.0 - \alpha$. This constraint makes $S_{Tv} \in [0, 1]$ commensurate with the range of the Dice coefficient. In this way, α and β become the balancing weights between FP and FN.

In the bottom row of Fig. 3 (b), it shows that the effect of the undersegmentation is less reflected in the Tversky loss function with higher α (i.e., lower β). In an extreme case $\alpha = 1.0$, the Tversky loss becomes 0.0 that undersegmentation is considered to be the same as perfect segmentation. On the other hand, the effect of the oversegmentation is less reflected in the Tversky loss function with lower α as shown in Fig. 3 (c). In both cases, the soft Dice loss stays the same because the effects of FP and FN are equally considered. The Tversky loss function returns 0.0 regardless of the choice of α for the correct and balanced segmentation as shown in Fig. 3 (d). This is highly desirable for our purpose for the segmentation probability estimation since we do not want to penalize the balanced segmentation.

We enforce a network to learn to under-/over-segment by varying α and β : i.e., $\alpha > \beta$ to undersegment and $\alpha < \beta$ to oversegment. Note that the same purpose can be achieved by manipulating weights of the log losses of positive and negative labels in the binary cross-entropy function [8]. We chose the Tversky loss because it was normalized nicely and shown to perform well for medical image segmentation.

3. Ensemble with Varying Tversky Loss

One straightforward approach to estimate the segmentation probability maps with the varying Tversky loss is the network ensembles with multiple networks trained with varying Tversky loss hyperparameters, α and β [16].

For a standard DL approach, a segmentation probability estimation function $f(\mathbf{I}|\boldsymbol{\theta}) = p(\mathbf{y}; \boldsymbol{\theta})$ estimates the segmentation probability map $p(\mathbf{y}; \boldsymbol{\theta})$ conditioned on the network $\boldsymbol{\theta}$ from an image \mathbf{I} . The ensemble approach with multiple networks $\Theta = \{\boldsymbol{\theta}_1, \dots, \boldsymbol{\theta}_{N_e}\}$ is formulated as follows,

$$f_{ens}(\mathbf{I}) = \int f(\mathbf{I}|\boldsymbol{\theta})p(\boldsymbol{\theta})d\boldsymbol{\theta} \quad (5)$$

$$= \frac{1}{N_e} \sum_{i=1}^{N_e} f(\mathbf{I}|\boldsymbol{\theta}_i), \text{ if } p(\boldsymbol{\theta}_i) = \frac{1}{N_e}, \forall i, \quad (6)$$

where N_e is the number of the individual networks.

Let $\mathbf{H} = \{\mathbf{h}_1, \dots, \mathbf{h}_{N_e}\}$ and $\Theta = \{\boldsymbol{\theta}_1, \dots, \boldsymbol{\theta}_{N_e}\}$ be the sets of varying Tversky loss hyperparameters, $\mathbf{h}_i = (\alpha_i, \beta_i)$, and the DL networks determined by the corresponding \mathbf{h}_i , respectively. The hyperparameter \mathbf{h} is in the 1-simplex because of the constraint, $0 \leq \alpha_i \leq 1, \beta_i = 1 - \alpha_i$. The network $\boldsymbol{\theta}_i$ is trained to penalize less on undersegmentation with $\alpha_i > \beta_i$, and less on oversegmentation with $\beta_i > \alpha_i$. The segmentation probability estimation of each network is now conditioned on the hyperparameters \mathbf{h}_i since an individual network $\boldsymbol{\theta}_i$ is trained with the Tversky loss $L_{Tv}(\cdot; \mathbf{h}_i)$,

$$f(\mathbf{I}; \boldsymbol{\theta}_i|\mathbf{h}_i) = p(\mathbf{y}; \boldsymbol{\theta}_i|\mathbf{h}_i). \quad (7)$$

The ensemble function f_{ens} is defined as follows,

$$f_{ens}(\mathbf{I}) = \frac{1}{N_e} \sum_{i=1}^{N_e} f(\mathbf{I}; \boldsymbol{\theta}_i|\mathbf{h}_i). \quad (8)$$

It is the discrete version of $p_{ens}(\mathbf{y}) = \int p(\mathbf{y}; \boldsymbol{\theta}|\mathbf{h})p(\mathbf{h})d\mathbf{h}$ over \mathbf{h} when \mathbf{h} is uniformly distributed, i.e., $p(\mathbf{h}_i) = 1/N_e, \forall i = 1, \dots, N_e$.

Our approach relies on varying segmentation results estimated by DL networks conditioned on the varying Tversky loss without manipulating human annotations or any fixed priors on the segmentation labels to leverage the flexibility of DL networks on segmentation. One drawback of our ensemble method is that it requires high computational resources to train multiple networks. Typically, the number of individual networks for the ensemble is limited (e.g., three to five) which is not optimal for the probability estimation.

4. Hypernetwork Ensemble

4.1. Hypernetwork Architecture

The hypernetwork architecture in our framework is adapted from the hypernetwork in [20] and the residual UNet in [28]. Fig. 4 illustrates the overall architecture of the proposed hypernetwork. The mapping network $\boldsymbol{\theta}_m$ generates the hypervector \mathbf{z}_h from the hyperparameter $\mathbf{h} = (\alpha, \beta)$. The mapping network consists of dense layers and rectifying linear units (ReLU) [20,25].

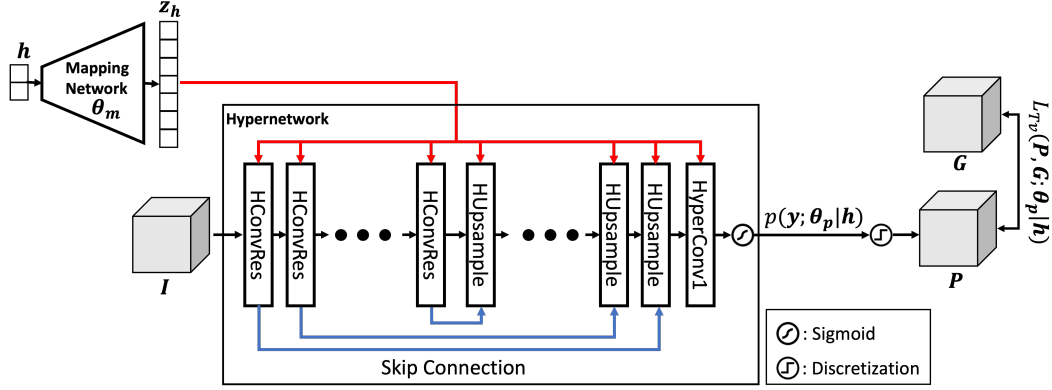


Figure 4. Hypernetwork architecture. The hypervector z_h mapped by the mapping network θ_m from a hyperparameter h is used to generate the parameters of the primary ResUNet network θ_p in the hyperconvolution residual (HConvRes) and upsample (HUpsample) blocks. The primary network takes an image I and estimate the segmentation label map P . The final feature output of θ_p is transformed to the segmentation probability map $p(y; \theta_p|h)$ by the sigmoid and discretized to P . During training, the loss is calculated by the Tversky loss with the hyperparameter h between P and a human annotation G .

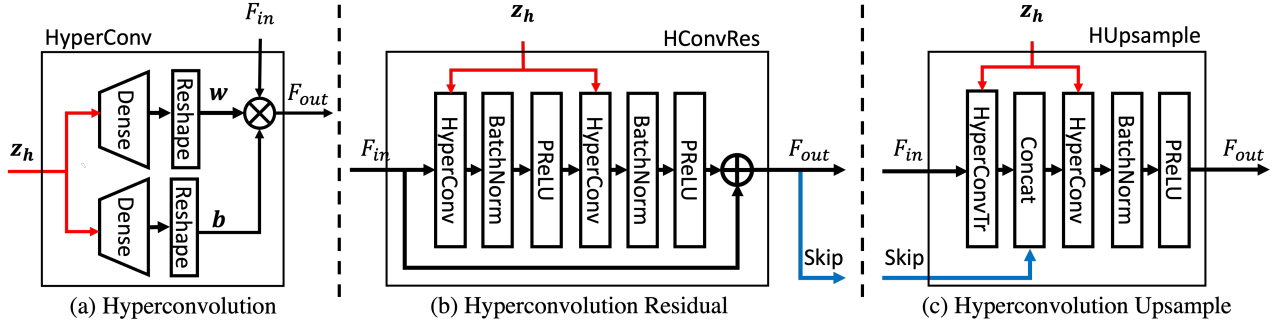


Figure 5. Hyperblocks. (a) The hyperconvolution (HyperConv) block estimates the kernel weights w and biases b of the convolution block of the primary network via the separate dense layers. (b) The HyperConv residual unit (HConvRes) for the encoding part of the primary network is the sequence of the HyperConv, batch normalization, and PReLU. (c) The hyperupsample (HUpsample) for the decoder consists of the transposed HyperConv (HyperConvTr), concatenation, HyperConv, batch normalization, and PReLU.

The hypernetwork consists of hyperconvolution residual (HConvRes) and hyperconvolution upsample (HUpsample) units with skip connections that constitute the ResUNet architecture with the hyperconvolution (HyperConv) blocks substituting the standard convolution blocks [20, 28, 37, 53]. The HyperConv block is illustrated in Fig. 5 (a). There are two single dense layers that take the mapped hypervector z_h as an input. Those dense layers estimate the kernel weight w and bias b for the convolution. The input feature F_{in} is convolved with the generated w and b . The parameters of the dense layers and the generated parameters of the convolution blocks constitute the hypernetwork θ_h and the primary network θ_p , respectively. The transposed HyperConv (HyperConvTr) is similar to the HyperConv block with the transposed shape of w and the transposed convolution function instead of the convolution function. The HConvRes and HUpsample units are illustrated in Fig. 5 (b) and (c), respectively. The residual and upsample structures with the

skip connection are adapted from [28] with the parametric rectifying linear units (PReLUs) and the batch normalization [18, 53, 70]. The hypernetwork parameters θ_h are trainable parameters while the parameters of the primary segmentation network θ_p are conditioned on the hyperparameters h and generated by θ_h . After the encoding and decoding steps, the features are convolved with the $1 \times 1 \times 1$ HyperConv block followed by the sigmoid function to generate a segmentation probability map $p(y; \theta_p|h)$.

At the training stage, the final segmentation label map P is obtained by discretizing the the segmentation probability map by simple thresholding for binary segmentation. We used the Tversky loss function $L_{Tv}(P, G; h)$ in Eq. 4 with randomly sampled $h=(\alpha, \beta)$ where $\alpha \sim U(\epsilon, 1 - \epsilon)$, $\beta = 1 - \alpha$ for each minibatch as a training loss function. ϵ is the small value to guarantee computational stability. We set $\epsilon=0.05$ for experiments.

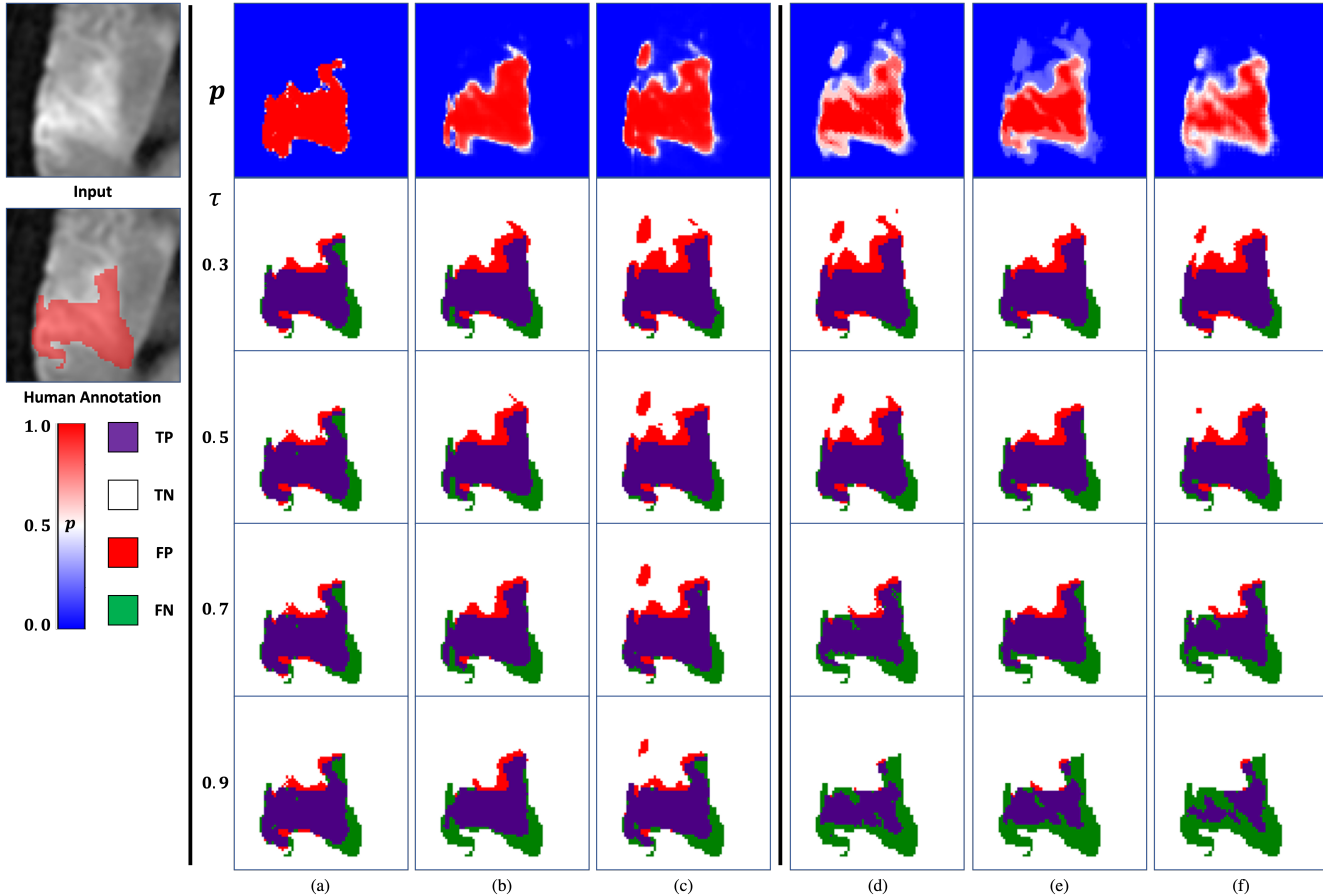


Figure 6. Binary segmentation results with varying probability thresholds τ . The probability maps estimated by (a) UNETR, (b) UNETR with dropout, (c) UNETR ensemble with random data subsets, (d) our ResUNet ensemble with varying Tversky loss (V-Tv), (e) UNETR ensemble with V-Tv, and (f) hypernetwork ensemble methods. Our methods (e-f) captured the underlying lesion structure.

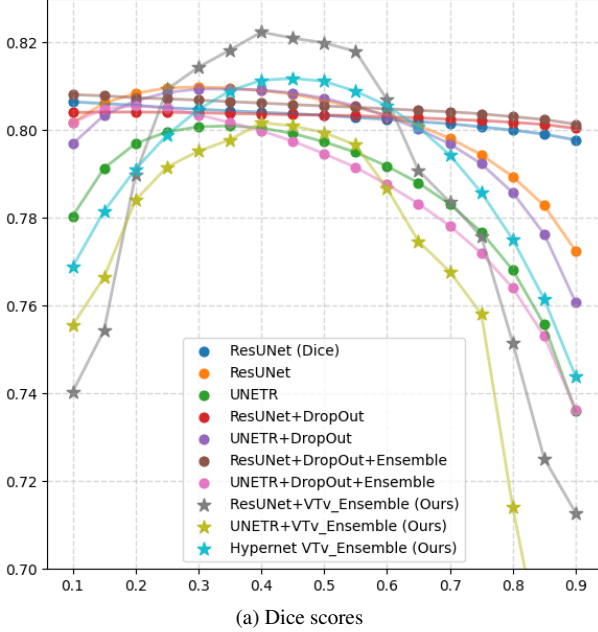
		Dice	Bal. Acc.	Precision	Recall	ROC AUC	Training Time (GPU Hours)
Baselines	ResUNet (Dice)	0.803	0.873	0.869	0.747	0.822	7
	ResUNet	0.807	0.876	0.870	0.752	0.856	8
	UNETR	0.797	0.865	0.878	0.730	0.851	38
Dropout	ResUNet	0.803	0.882	0.848	0.763	0.819	8
	UNETR	0.807	0.871	0.884	0.743	0.857	57
Ensemble	ResUNet	0.806	0.874	0.873	0.747	0.823	37
	UNETR	0.795	0.855	0.904	0.709	0.854	190
Ensemble w. VTv (Ours)	ResUNet	0.820	0.888	0.868	0.776	0.884	53
	UNETR	0.799	0.872	0.862	0.745	0.863	258
Hypernet w. VTv (Ours)	HyperUNet	0.811	0.891	0.842	0.783	0.869	13

Table 1. Binary segmentation results with the fixed probability threshold (0.5) and the training time (GPU hours). The best performance metrics are bold-faced.

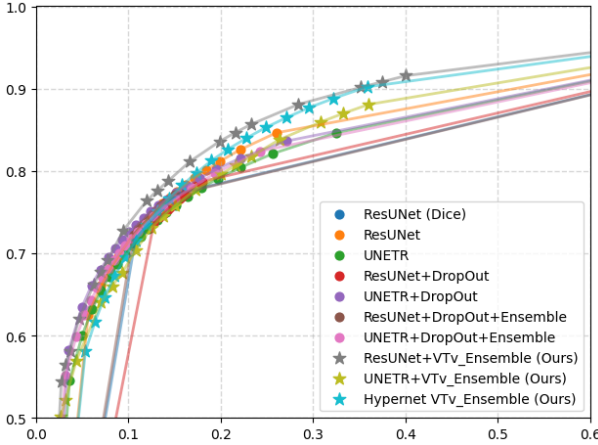
4.2. Hypernetwork Ensemble

The ensemble process with the hypernetwork is similar to the network ensemble strategy with the varying Tversky loss described in Section 3. The advantage of the hyper-

network ensemble over the network ensemble strategy is that we can sample hyperparameters h with any intervals with a single hypernetwork because the the hypernetwork is trained on continuously sampled h at the cost of the in-



(a) Dice scores



(b) ROC curves

Figure 7. (a) Dice and (b) receiver operating curves (ROC) with varying probability thresholds. The proposed ResUNet ensemble (gray stars) and the hypernetwork (cyan stars) ensemble with the varying Tversky loss showed the best performance.

creased inference time proportional to the number of h for the ensemble, $O(N_e)$. The set of multiple DL networks Θ in Eq. 8 is now replaced with the estimated parameters of the primary segmentation network θ_p determined by h_i ,

$$f_{hyper}(\mathbf{I}) = \frac{1}{N_e} \sum_{i=1}^{N_e} f(\mathbf{I}; \theta_p | h_i). \quad (9)$$

Finally, the segmentation probability map $p(\mathbf{y})$, estimated by $f_{hyper}(\mathbf{I}) = p(\mathbf{y})$, is binarized by thresholding to generate a binary segmentation label map.

5. Experiments

Dataset We applied our proposed methods to the acute ischemic stroke lesion segmentation problem with clinical-grade 3D diffusion weighted images (DWIs) from the MRI-GENIE study [14]. The informed and written consent forms were obtained from all patients or their legal representatives [14, 46]. Each hospital received approval of their internal review board [14]. Five hundreds and fifty images with human expert annotations were used in our experiments. We divide the data set to 412 ($\sim 75\%$) training data and 138 ($\sim 25\%$) validation data. All images were center-aligned and resampled to $1.0 \times 1.0 \times 6.0 \text{ mm}^3$ ($256 \times 256 \times 32 \text{ vox}$). The intensity range of each image was scaled to $[0, 1]$.

Configurations We compared the Residual UNet (ResUNet) [28, 53] and the multi-head transformer-based method (UNETR) [17] that showed the state-of-the-art performance for 3D medical images to our methods. We trained the ResUNet and UNETR in three configurations: 1) the *vanilla* setting, 2) dropout with the rate of 0.1, and 3) the network ensembles with 5-fold training subsets. We trained all comparison methods with the Dice cross-entropy (CE) loss [63]. One vanilla ResUNet was trained with the soft Dice loss as a baseline [9]. Our network ensemble approach with the varying Tversky (V-Tv) loss used the separate ensembles of five individual ResUNet and UNETR networks with the same training set to eliminate the effect of random data. We trained individual networks with the Tversky loss hyperparameters $\alpha = \{0.1, 0.3, 0.5, 0.7, 0.9\}$.

Implementation Details For all configurations, images and annotation labels were randomly cropped to $192 \times 192 \times 16$ patches. At the inference stage, the segmentation probability maps and label maps were predicted by the sliding windows technique with 80% overlap [27]. We optimized all configurations except the hypernetwork approach with the Adam optimizer with the learning rate $1e^{-4}$ and the weight decay $1e^{-3}$ [29]. The hypernetwork was trained with the learning rate $1e^{-5}$ and the weight decay $1e^{-3}$ for training stability. We implemented our hypernetwork architecture with the MONAI 0.7.0 and PyTorch 1.9 frameworks¹ [51, 64]. We used one NVIDIA Titan Xp with 12 GB GPU memory per network for training and inference.

5.1. Segmentation Probability Estimation

Fig. 2 and the top row of Fig. 6 show the examples of the estimated segmentation probability maps. In Fig. 2, the segmentation probability maps of a validation image (Fig. 2 (a)) with a human annotation (Fig. 2 (b)) estimated by the vanilla ResUNet, UNETR with the dropout, UNETR ensembles with Dice CE loss with data subsets, and our proposed UNETR ensemble with the V-Tv loss and hypernetwork ensemble approach (Fig. 2 (c-g), respectively) are pre-

¹<https://monai.io/>, <https://pytorch.org/>

sented. The segmentation probability maps estimated by the other methods were highly polarized to 0.0 and 1.0 which did not reflect the ambiguity. At the bottom of Figure 2, an ambiguous area (yellow circle) between the stroke lesions was segmented as stroke lesions with high confidence while the area is the white matter hyperintensity (WMH) which is different from stroke lesions. Our approaches estimated the probability close to 0.5 for the area that indicated the ambiguity between WMH and lesions. The example in the top row shows the strength of our method for the ambiguity between lesion and possible image artifact (yellow circle). The qualitative example shown in Fig. 6 shows the strength of our approaches that we can control the binary segmentation results with different probability thresholds. Our estimated probability maps captured the highly probable area of lesions as shown in the input image on the left column with the high probability threshold (the bottom row Fig. 6 (d-f)). Different thresholds affected the results from the other methods insignificantly (Fig. 6 (a-c)).

Fig. 7 (a) shows the curves of aggregated Dice scores over different probability thresholds. Because there is the inherent ambiguity in our human annotations, higher Dice scores can be relatively less important in our evaluation than the other segmentation tasks. However, our proposed ResUNet ensemble with the V-Tv loss and hypernetwork methods (marked by stars) outperformed the other methods (marked by circles). The important characteristic of the proposed methods shown in the Dice curves is that the Dice score changes smoothly over probability thresholds. This aligns well with the intuition that the higher probability thresholds would lead to undersegmentation and the lower to oversegmentation when the *true* probability map is given. As shown in Fig. 6, this property gives the control to users that they can decide the level of under-/over-segmentation.

The receiver operating characteristic (ROC) curves in Fig. 7 (b) shows how the false positive rates (FPR) and the true positive rates (TPR) are distributed with the same 0.05 probability threshold interval for the proposed methods (marked by stars) and the other methods (marked by circles). More densely clustered FPR-TPR points with varying thresholds of the other approaches indicated the more polarized segmentation probability estimation. The proposed ResNet ensemble with the V-Tv loss achieved the best area under curve of the ROC (ROC-AUC) followed by the hypernetwork ensemble as shown in Table 1. Because of the imbalanced ratios of positive and negative labels (i.e., smaller lesion volumes compared to the whole brain), the TPR and FPR did not go smoothly to 1.0 for all methods.

5.2. Binary Segmentation Results

We compared the binary segmentation results by setting the segmentation probability threshold to 0.5. Table 1 summarizes the evaluation metrics of the proposed and the other

methods. The proposed ResUNet ensemble with the V-Tv loss achieved the best performances on the aggregated Dice score (0.82) and ROC-AUC (0.884). The hypernetwork ensemble achieved the best performance on the balanced accuracy (0.891) and recall (0.783) and the second best on the ROC-AUC (0.869). The UNETR ensembles with the random data subsets achieved the best precision (0.904). Its relatively low recall (0.709) may indicate that it enforced undersegmentation. The binary segmentation results showed that our methods did not sacrifice the performance on the binary segmentation in the full-automated scenario. They marginally improved the results compared to the state-of-the-arts. The training time of the hypernetwork (13 GPU hours) was lower than those of the ensemble methods and UNETRs although it was higher than those of the training of individual ResUNETs.

6. Discussion

We proposed novel approaches to improve the segmentation probability map estimation by leveraging the network and hypernetwork ensembles with the varying Tversky loss [15, 16, 20, 57, 71]. The proposed methods successfully estimated the underlying segmentation probability maps that reflected the ambiguity for the challenging medical image segmentation task without sacrificing the binary segmentation performance compared to the state-of-the-arts. Although our approaches were only tested on the binary 3D image segmentation problem, our proposed approaches can be easily extended to wider applications.

There are a few limitations of the proposed methods. The proposed hypernetwork architecture is implemented with the fully-connected dense layers [54] in the HyperConv block that inflated the size of the hypernetwork. This can be addressed by employing the efficient encoder designs [30, 34, 53]. The quality of the estimated segmentation probability maps were not quantitatively evaluated due to the lack of multiple annotations per image in our dataset. The alternative approach can be the generalized energy distance [33, 39, 48]. Also, it can be evaluated semi-quantitatively by the human expert rejection rate often used for an ambiguous segmentation problem [5]. Lastly, our experiments did not cover the stochastic networks [33, 39, 48]. Although they focused on the generation of the multiple segmentation label candidates and the estimation of the segmentation uncertainty, the segmentation probability map can be obtained by averaging the generated candidates at inference that can be comparable to ours.

We believe our methods can contribute to many segmentation problems, not only limited to medical applications, that suffer from the inherent label ambiguity and the segmentation probability maps are highly desirable.

Acknowledgements This research was supported by NIH NINDS MRI-GENIE: R01NS086905, K23NS064052, R01NS082285, NIH NIBIB NAC P41EB015902 and NIH NINDS U19NS115388.

References

- [1] Nabila Abraham and Naimul Mefraz Khan. A novel focal tversky loss function with improved attention u-net for lesion segmentation. In *2019 IEEE 16th International Symposium on Biomedical Imaging (ISBI 2019)*, pages 683–687. IEEE, 2019. **3**
- [2] DeWitt C Baldwin Jr and Steven R Daugherty. Sleep deprivation and fatigue in residency training: results of a national survey of first-and second-year residents. *Sleep*, 27(2):217–223, 2004. **1**
- [3] Christian F Baumgartner, Kerem C Tezcan, Krishna Chaitanya, Andreas M Hötter, Urs J Muehlethaler, Khoschy Schawkat, Anton S Becker, Olivio Donati, and Ender Konukoglu. Phiseg: Capturing uncertainty in medical image segmentation. In *International Conference on Medical Image Computing and Computer-Assisted Intervention*, pages 119–127. Springer, 2019. **2**
- [4] Jeroen Bertels, David Robben, Dirk Vandermeulen, and Paul Suetens. Optimization with soft dice can lead to a volumetric bias. In *International MICCAI Brainlesion Workshop*, pages 89–97. Springer, 2019. **3**
- [5] Benjamin Billot, Martina Bocchetta, Emily Todd, Adrian V Dalca, Jonathan D Rohrer, and Juan Eugenio Iglesias. Automated segmentation of the hypothalamus and associated subunits in brain mri. *Neuroimage*, 223:117287, 2020. **8**
- [6] Benjamin Billot, Eleanor Robinson, Adrian V Dalca, and Juan Eugenio Iglesias. Partial volume segmentation of brain mri scans of any resolution and contrast. In *International Conference on Medical image computing and computer-assisted intervention*, pages 177–187. Springer, 2020. **1**
- [7] Minghao Chen, Jianlong Fu, and Haibin Ling. One-shot neural ensemble architecture search by diversity-guided search space shrinking. In *Proceedings of the IEEE/CVF Conference on Computer Vision and Pattern Recognition*, pages 16530–16539, 2021. **2, 3**
- [8] David R Cox. The regression analysis of binary sequences. *Journal of the Royal Statistical Society: Series B (Methodological)*, 20(2):215–232, 1958. **4**
- [9] Lee R Dice. Measures of the amount of ecologic association between species. *Ecology*, 26(3):297–302, 1945. **4, 7**
- [10] Bruce Fischl. Freesurfer. *Neuroimage*, 62(2):774–781, 2012. **2**
- [11] Bruce Fischl, David H Salat, Evelina Busa, Marilyn Albert, Megan Dieterich, Christian Haselgrove, Andre Van Der Kouwe, Ron Killiany, David Kennedy, Shuna Klavenness, et al. Whole brain segmentation: automated labeling of neuroanatomical structures in the human brain. *Neuron*, 33(3):341–355, 2002. **1**
- [12] MA Ganaie, Minghui Hu, et al. Ensemble deep learning: A review. *arXiv preprint arXiv:2104.02395*, 2021. **2, 3**
- [13] Timur Garipov, Pavel Izmailov, Dmitrii Podoprikin, Dmitry Vetrov, and Andrew Gordon Wilson. Loss surfaces, mode connectivity, and fast ensembling of dnns. In *Proceedings of the 32nd International Conference on Neural Information Processing Systems*, pages 8803–8812, 2018. **2, 3**
- [14] Anne-Katrin Giese, Markus D Schirmer, Kathleen L Donahue, Lisa Cloonan, Robert Irie, Stefan Winzeck, Mark JRJ Bouts, Elissa C McIntosh, Steven J Mocking, Adrian V Dalca, et al. Design and rationale for examining neuroimaging genetics in ischemic stroke: The mri-genie study. *Neurology Genetics*, 3(5), 2017. **1, 2, 7**
- [15] David Ha, Andrew Dai, and Quoc V Le. Hypernetworks. *arXiv preprint arXiv:1609.09106*, 2016. **2, 3, 8**
- [16] Lars Kai Hansen and Peter Salamon. Neural network ensembles. *IEEE transactions on pattern analysis and machine intelligence*, 12(10):993–1001, 1990. **2, 3, 4, 8**
- [17] Ali Hatamizadeh, Yucheng Tang, Vishwesh Nath, Dong Yang, Andriy Myronenko, Bennett Landman, Holger Roth, and Daguang Xu. Unetr: Transformers for 3d medical image segmentation. *arXiv preprint arXiv:2103.10504*, 2021. **3, 7**
- [18] Kaiming He, Xiangyu Zhang, Shaoqing Ren, and Jian Sun. Delving deep into rectifiers: Surpassing human-level performance on imagenet classification. In *Proceedings of the IEEE international conference on computer vision*, pages 1026–1034, 2015. **5**
- [19] Emily J Herron, Steven R Young, and Thomas E Potok. Ensembles of networks produced from neural architecture search. In *International Conference on High Performance Computing*, pages 223–234. Springer, 2020. **2, 3**
- [20] Andrew Hoopes, Malte Hoffmann, Bruce Fischl, John Guttag, and Adrian V Dalca. Hypermorph: Amortized hyperparameter learning for image registration. In *International Conference on Information Processing in Medical Imaging*, pages 3–17. Springer, 2021. **2, 3, 4, 5, 8**
- [21] Gao Huang, Yu Sun, Zhuang Liu, Daniel Sedra, and Kilian Q Weinberger. Deep networks with stochastic depth. In *European conference on computer vision*, pages 646–661. Springer, 2016. **2, 3**
- [22] Wei Ji, Shuang Yu, Junde Wu, Kai Ma, Cheng Bian, Qi Bi, Jingjing Li, Hanruo Liu, Li Cheng, and Yefeng Zheng. Learning calibrated medical image segmentation via multi-rater agreement modeling. In *Proceedings of the IEEE/CVF Conference on Computer Vision and Pattern Recognition*, pages 12341–12351, 2021. **2**
- [23] Xu Jia, Bert De Brabandere, Tinne Tuytelaars, and Luc V Gool. Dynamic filter networks. *Advances in neural information processing systems*, 29:667–675, 2016. **3**
- [24] Konstantinos Kamnitsas, Enzo Ferrante, Sarah Parisot, Christian Ledig, Aditya V Nori, Antonio Criminisi, Daniel Rueckert, and Ben Glocker. Deepmedic for brain tumor segmentation. In *International workshop on Brainlesion: Glioma, multiple sclerosis, stroke and traumatic brain injuries*, pages 138–149. Springer, 2016. **3**
- [25] Tero Karras, Samuli Laine, and Timo Aila. A style-based generator architecture for generative adversarial networks. In *Proceedings of the IEEE/CVF Conference on Computer Vision and Pattern Recognition*, pages 4401–4410, 2019. **4**
- [26] Alex Kendall, Vijay Badrinarayanan, and Roberto Cipolla. Bayesian segnet: Model uncertainty in deep convolutional neural networks. In *Proceedings of the IEEE conference on computer vision and pattern recognition*, pages 748–756, 2015. **2, 3, 4, 5, 6, 7, 8, 9, 10, 11, 12, 13, 14, 15, 16, 17, 18, 19, 20, 21, 22, 23, 24, 25, 26, 27, 28, 29, 30, 31, 32, 33, 34, 35, 36, 37, 38, 39, 40, 41, 42, 43, 44, 45, 46, 47, 48, 49, 50, 51, 52, 53, 54, 55, 56, 57, 58, 59, 60, 61, 62, 63, 64, 65, 66, 67, 68, 69, 70, 71, 72, 73, 74, 75, 76, 77, 78, 79, 80, 81, 82, 83, 84, 85, 86, 87, 88, 89, 90, 91, 92, 93, 94, 95, 96, 97, 98, 99, 100, 101, 102, 103, 104, 105, 106, 107, 108, 109, 110, 111, 112, 113, 114, 115, 116, 117, 118, 119, 120, 121, 122, 123, 124, 125, 126, 127, 128, 129, 130, 131, 132, 133, 134, 135, 136, 137, 138, 139, 140, 141, 142, 143, 144, 145, 146, 147, 148, 149, 150, 151, 152, 153, 154, 155, 156, 157, 158, 159, 160, 161, 162, 163, 164, 165, 166, 167, 168, 169, 170, 171, 172, 173, 174, 175, 176, 177, 178, 179, 180, 181, 182, 183, 184, 185, 186, 187, 188, 189, 190, 191, 192, 193, 194, 195, 196, 197, 198, 199, 200, 201, 202, 203, 204, 205, 206, 207, 208, 209, 210, 211, 212, 213, 214, 215, 216, 217, 218, 219, 220, 221, 222, 223, 224, 225, 226, 227, 228, 229, 230, 231, 232, 233, 234, 235, 236, 237, 238, 239, 240, 241, 242, 243, 244, 245, 246, 247, 248, 249, 250, 251, 252, 253, 254, 255, 256, 257, 258, 259, 260, 261, 262, 263, 264, 265, 266, 267, 268, 269, 270, 271, 272, 273, 274, 275, 276, 277, 278, 279, 280, 281, 282, 283, 284, 285, 286, 287, 288, 289, 290, 291, 292, 293, 294, 295, 296, 297, 298, 299, 300, 301, 302, 303, 304, 305, 306, 307, 308, 309, 310, 311, 312, 313, 314, 315, 316, 317, 318, 319, 320, 321, 322, 323, 324, 325, 326, 327, 328, 329, 330, 331, 332, 333, 334, 335, 336, 337, 338, 339, 340, 341, 342, 343, 344, 345, 346, 347, 348, 349, 350, 351, 352, 353, 354, 355, 356, 357, 358, 359, 360, 361, 362, 363, 364, 365, 366, 367, 368, 369, 370, 371, 372, 373, 374, 375, 376, 377, 378, 379, 380, 381, 382, 383, 384, 385, 386, 387, 388, 389, 390, 391, 392, 393, 394, 395, 396, 397, 398, 399, 400, 401, 402, 403, 404, 405, 406, 407, 408, 409, 410, 411, 412, 413, 414, 415, 416, 417, 418, 419, 420, 421, 422, 423, 424, 425, 426, 427, 428, 429, 430, 431, 432, 433, 434, 435, 436, 437, 438, 439, 440, 441, 442, 443, 444, 445, 446, 447, 448, 449, 450, 451, 452, 453, 454, 455, 456, 457, 458, 459, 460, 461, 462, 463, 464, 465, 466, 467, 468, 469, 470, 471, 472, 473, 474, 475, 476, 477, 478, 479, 480, 481, 482, 483, 484, 485, 486, 487, 488, 489, 490, 491, 492, 493, 494, 495, 496, 497, 498, 499, 500, 501, 502, 503, 504, 505, 506, 507, 508, 509, 510, 511, 512, 513, 514, 515, 516, 517, 518, 519, 520, 521, 522, 523, 524, 525, 526, 527, 528, 529, 530, 531, 532, 533, 534, 535, 536, 537, 538, 539, 540, 541, 542, 543, 544, 545, 546, 547, 548, 549, 550, 551, 552, 553, 554, 555, 556, 557, 558, 559, 560, 561, 562, 563, 564, 565, 566, 567, 568, 569, 570, 571, 572, 573, 574, 575, 576, 577, 578, 579, 580, 581, 582, 583, 584, 585, 586, 587, 588, 589, 590, 591, 592, 593, 594, 595, 596, 597, 598, 599, 600, 601, 602, 603, 604, 605, 606, 607, 608, 609, 610, 611, 612, 613, 614, 615, 616, 617, 618, 619, 620, 621, 622, 623, 624, 625, 626, 627, 628, 629, 630, 631, 632, 633, 634, 635, 636, 637, 638, 639, 640, 641, 642, 643, 644, 645, 646, 647, 648, 649, 650, 651, 652, 653, 654, 655, 656, 657, 658, 659, 660, 661, 662, 663, 664, 665, 666, 667, 668, 669, 670, 671, 672, 673, 674, 675, 676, 677, 678, 679, 680, 681, 682, 683, 684, 685, 686, 687, 688, 689, 690, 691, 692, 693, 694, 695, 696, 697, 698, 699, 700, 701, 702, 703, 704, 705, 706, 707, 708, 709, 710, 711, 712, 713, 714, 715, 716, 717, 718, 719, 720, 721, 722, 723, 724, 725, 726, 727, 728, 729, 730, 731, 732, 733, 734, 735, 736, 737, 738, 739, 740, 741, 742, 743, 744, 745, 746, 747, 748, 749, 750, 751, 752, 753, 754, 755, 756, 757, 758, 759, 760, 761, 762, 763, 764, 765, 766, 767, 768, 769, 770, 771, 772, 773, 774, 775, 776, 777, 778, 779, 780, 781, 782, 783, 784, 785, 786, 787, 788, 789, 790, 791, 792, 793, 794, 795, 796, 797, 798, 799, 800, 801, 802, 803, 804, 805, 806, 807, 808, 809, 810, 811, 812, 813, 814, 815, 816, 817, 818, 819, 820, 821, 822, 823, 824, 825, 826, 827, 828, 829, 830, 831, 832, 833, 834, 835, 836, 837, 838, 839, 840, 841, 842, 843, 844, 845, 846, 847, 848, 849, 850, 851, 852, 853, 854, 855, 856, 857, 858, 859, 860, 861, 862, 863, 864, 865, 866, 867, 868, 869, 870, 871, 872, 873, 874, 875, 876, 877, 878, 879, 880, 881, 882, 883, 884, 885, 886, 887, 888, 889, 890, 891, 892, 893, 894, 895, 896, 897, 898, 899, 900, 901, 902, 903, 904, 905, 906, 907, 908, 909, 910, 911, 912, 913, 914, 915, 916, 917, 918, 919, 920, 921, 922, 923, 924, 925, 926, 927, 928, 929, 930, 931, 932, 933, 934, 935, 936, 937, 938, 939, 940, 941, 942, 943, 944, 945, 946, 947, 948, 949, 950, 951, 952, 953, 954, 955, 956, 957, 958, 959, 960, 961, 962, 963, 964, 965, 966, 967, 968, 969, 970, 971, 972, 973, 974, 975, 976, 977, 978, 979, 980, 981, 982, 983, 984, 985, 986, 987, 988, 989, 990, 991, 992, 993, 994, 995, 996, 997, 998, 999, 1000.**

- tional encoder-decoder architectures for scene understanding. *arXiv preprint arXiv:1511.02680*, 2015. [2](#)
- [27] Eamonn Keogh, Selina Chu, David Hart, and Michael Paz-zani. An online algorithm for segmenting time series. In *Proceedings 2001 IEEE international conference on data mining*, pages 289–296. IEEE, 2001. [7](#)
- [28] Eric Kerfoot, James Clough, Ilkay Oksuz, Jack Lee, Andrew P King, and Julia A Schnabel. Left-ventricle quantification using residual u-net. In *International Workshop on Statistical Atlases and Computational Models of the Heart*, pages 371–380. Springer, 2018. [4](#), [5](#), [7](#)
- [29] Diederik P Kingma and Jimmy Ba. Adam: A method for stochastic optimization. *arXiv preprint arXiv:1412.6980*, 2014. [7](#)
- [30] Diederik P Kingma and Max Welling. Auto-encoding variational bayes. *arXiv preprint arXiv:1312.6114*, 2013. [8](#)
- [31] Sylwester Klocek, Łukasz Maziarka, Maciej Wołczyk, Jacek Tabor, Jakub Nowak, and Marek Śmieja. Hypernetwork functional image representation. In *International Conference on Artificial Neural Networks*, pages 496–510. Springer, 2019. [3](#)
- [32] Simon AA Kohl, Bernardino Romera-Paredes, Klaus H Maier-Hein, Danilo Jimenez Rezende, SM Eslami, Pushmeet Kohli, Andrew Zisserman, and Olaf Ronneberger. A hierarchical probabilistic u-net for modeling multi-scale ambiguities. *arXiv preprint arXiv:1905.13077*, 2019. [2](#)
- [33] Simon AA Kohl, Bernardino Romera-Paredes, Clemens Meyer, Jeffrey De Fauw, Joseph R Ledsam, Klaus H Maier-Hein, SM Eslami, Danilo Jimenez Rezende, and Olaf Ronneberger. A probabilistic u-net for segmentation of ambiguous images. *arXiv preprint arXiv:1806.05034*, 2018. [1](#), [8](#)
- [34] Mark A Kramer. Nonlinear principal component analysis using autoassociative neural networks. *AICHE journal*, 37(2):233–243, 1991. [8](#)
- [35] Anders Krogh, Jesper Vedelsby, et al. Neural network ensembles, cross validation, and active learning. *Advances in neural information processing systems*, 7:231–238, 1995. [2](#), [3](#)
- [36] Balaji Lakshminarayanan, Alexander Pritzel, and Charles Blundell. Simple and scalable predictive uncertainty estimation using deep ensembles. *Advances in neural information processing systems*, 30, 2017. [2](#)
- [37] Yann LeCun, Yoshua Bengio, et al. Convolutional networks for images, speech, and time series. *The handbook of brain theory and neural networks*, 3361(10):1995, 1995. [5](#)
- [38] Yann LeCun, Yoshua Bengio, and Geoffrey Hinton. Deep learning. *nature*, 521(7553):436–444, 2015. [1](#)
- [39] Stefan Lee, Senthil Purushwalkam Shiva Prakash, Michael Cogswell, Viresh Ranjan, David Crandall, and Dhruv Batra. Stochastic multiple choice learning for training diverse deep ensembles. In *Advances in Neural Information Processing Systems*, pages 2119–2127, 2016. [1](#), [8](#)
- [40] Hongwei Li, Gongfa Jiang, Jianguo Zhang, Ruixuan Wang, Zhaolei Wang, Wei-Shi Zheng, and Bjoern Menze. Fully convolutional network ensembles for white matter hyperintensities segmentation in mr images. *NeuroImage*, 183:650–665, 2018. [2](#), [3](#)
- [41] Xinxin Li, Yu Zhao, Jiyang Jiang, Jian Cheng, Wanlin Zhu, Zhenzhou Wu, Jing Jing, Zhe Zhang, Wei Wen, Perminder S Sachdev, et al. White matter hyperintensities segmentation using an ensemble of neural networks. *Human Brain Mapping*, 2021. [2](#), [3](#)
- [42] Xuan Liao, Wenhao Li, Qisen Xu, Xiangfeng Wang, Bo Jin, Xiaoyun Zhang, Yanfeng Wang, and Ya Zhang. Iteratively-refined interactive 3d medical image segmentation with multi-agent reinforcement learning. In *Proceedings of the IEEE/CVF Conference on Computer Vision and Pattern Recognition*, pages 9394–9402, 2020. [1](#)
- [43] Tsung-Yi Lin, Priya Goyal, Ross Girshick, Kaiming He, and Piotr Dollár. Focal loss for dense object detection. In *Proceedings of the IEEE international conference on computer vision*, pages 2980–2988, 2017. [3](#)
- [44] Gidi Littwin and Lior Wolf. Deep meta functionals for shape representation. In *Proceedings of the IEEE/CVF International Conference on Computer Vision*, pages 1824–1833, 2019. [3](#)
- [45] Tianyu Ma, Adrian V Dalca, and Mert R Sabuncu. Hyperconvolution networks for biomedical image segmentation. *arXiv preprint arXiv:2105.10559*, 2021. [3](#)
- [46] James F Meschia, Donna K Arnett, Hakan Ay, Robert D Brown Jr, Oscar R Benavente, John W Cole, Paul IW De Bakker, Martin Dichgans, Kimberly F Doheny, Myriam Fornage, et al. Stroke genetics network (sign) study: design and rationale for a genome-wide association study of ischemic stroke subtypes. *Stroke*, 44(10):2694–2702, 2013. [7](#)
- [47] Shervin Minaee, Yuri Y Boykov, Fatih Porikli, Antonio J Plaza, Nasser Kehtarnavaz, and Demetri Terzopoulos. Image segmentation using deep learning: A survey. *IEEE Transactions on Pattern Analysis and Machine Intelligence*, 2021. [1](#)
- [48] Miguel Monteiro, Loïc Le Folgoc, Daniel Coelho de Castro, Nick Pawłowski, Bernardo Marques, Konstantinos Kamnitsas, Mark van der Wilk, and Ben Glocker. Stochastic segmentation networks: Modelling spatially correlated aleatoric uncertainty. *arXiv preprint arXiv:2006.06015*, 2020. [1](#), [2](#), [8](#)
- [49] Yuval Nirkin, Lior Wolf, and Tal Hassner. Hyperseg: Patchwise hypernetwork for real-time semantic segmentation. In *Proceedings of the IEEE/CVF Conference on Computer Vision and Pattern Recognition*, pages 4061–4070, 2021. [3](#)
- [50] Ozan Oktay, Jo Schlemper, Loïc Le Folgoc, Matthew Lee, Mattias Heinrich, Kazunari Misawa, Kensaku Mori, Steven McDonagh, Nils Y Hammerla, Bernhard Kainz, et al. Attention u-net: Learning where to look for the pancreas. *arXiv preprint arXiv:1804.03999*, 2018. [3](#)
- [51] Adam Paszke, Sam Gross, Francisco Massa, Adam Lerer, James Bradbury, Gregory Chanan, Trevor Killeen, Zeming Lin, Natalia Gimelshein, Luca Antiga, Alban Desmaison, Andreas Kopf, Edward Yang, Zachary DeVito, Martin Raison, Alykhan Tejani, Sasank Chilamkurthy, Benoit Steiner, Lu Fang, Junjie Bai, and Soumith Chintala. Pytorch: An imperative style, high-performance deep learning library. In H. Wallach, H. Larochelle, A. Beygelzimer, F. d’Alché-Buc, E. Fox, and R. Garnett, editors, *Advances in Neural Information Processing Systems 32*, pages 8024–8035. Curran Associates, Inc., 2019. [7](#)

- [52] Dzung L Pham, Chenyang Xu, and Jerry L Prince. Current methods in medical image segmentation. *Annual review of biomedical engineering*, 2(1):315–337, 2000. [2](#)
- [53] Olaf Ronneberger, Philipp Fischer, and Thomas Brox. U-net: Convolutional networks for biomedical image segmentation. In *International Conference on Medical image computing and computer-assisted intervention*, pages 234–241. Springer, 2015. [1](#), [2](#), [5](#), [7](#), [8](#)
- [54] David E Rumelhart, Geoffrey E Hinton, and Ronald J Williams. Learning internal representations by error propagation. Technical report, California Univ San Diego La Jolla Inst for Cognitive Science, 1985. [8](#)
- [55] Christian Rupprecht, Iro Laina, Robert DiPietro, Maximilian Baust, Federico Tombari, Nassir Navab, and Gregory D Hager. Learning in an uncertain world: Representing ambiguity through multiple hypotheses. In *Proceedings of the IEEE International Conference on Computer Vision*, pages 3591–3600, 2017. [2](#)
- [56] Christos Sagonas, Georgios Tzimiropoulos, Stefanos Zafeiriou, and Maja Pantic. A semi-automatic methodology for facial landmark annotation. In *Proceedings of the IEEE conference on computer vision and pattern recognition workshops*, pages 896–903, 2013. [1](#), [2](#)
- [57] Seyed Sadegh Mohseni Salehi, Deniz Erdogmus, and Ali Gholipour. Tversky loss function for image segmentation using 3d fully convolutional deep networks. In *International workshop on machine learning in medical imaging*, pages 379–387. Springer, 2017. [2](#), [3](#), [4](#), [8](#)
- [58] Dinggang Shen, Guorong Wu, and Heung-Il Suk. Deep learning in medical image analysis. *Annual review of biomedical engineering*, 19:221–248, 2017. [2](#), [3](#)
- [59] Marine Soret, Stephen L Bacharach, and Irene Buvat. Partial-volume effect in pet tumor imaging. *Journal of nuclear medicine*, 48(6):932–945, 2007. [1](#)
- [60] Nitish Srivastava, Geoffrey Hinton, Alex Krizhevsky, Ilya Sutskever, and Ruslan Salakhutdinov. Dropout: a simple way to prevent neural networks from overfitting. *The journal of machine learning research*, 15(1):1929–1958, 2014. [2](#), [3](#)
- [61] Vaanathi Sundaresan, Giovanna Zamboni, Peter M Rothwell, Mark Jenkinson, and Ludovica Griffanti. Triplanar ensemble u-net model for white matter hyperintensities segmentation on mr images. *Medical image analysis*, 73:102184, 2021. [2](#), [3](#)
- [62] Saeid Asgari Taghanaki, Kumar Abhishek, Joseph Paul Cohen, Julien Cohen-Adad, and Ghassan Hamarneh. Deep semantic segmentation of natural and medical images: a review. *Artificial Intelligence Review*, 54(1):137–178, 2021. [1](#)
- [63] Saeid Asgari Taghanaki, Yefeng Zheng, S Kevin Zhou, Bogdan Georgescu, Puneet Sharma, Daguang Xu, Dorin Comaniciu, and Ghassan Hamarneh. Combo loss: Handling input and output imbalance in multi-organ segmentation. *Computerized Medical Imaging and Graphics*, 75:24–33, 2019. [7](#)
- [64] The MONAI Consortium. The MONAI Project. *Zenodo*, 2020. [7](#)
- [65] Götz Thomalla, Bastian Cheng, Martin Ebinger, Qing Hao, Thomas Tourdias, Ona Wu, Jong S Kim, Lorenz Breuer, Oliver C Singer, Steven Warach, et al. Dwi-flair mismatch for the identification of patients with acute ischaemic stroke within 4–5 h of symptom onset (pre-flair): a multicentre observational study. *The Lancet Neurology*, 10(11):978–986, 2011. [1](#)
- [66] Amos Tversky. Features of similarity. *Psychological review*, 84(4):327, 1977. [4](#)
- [67] Alan Q Wang, Adrian V Dalca, and Mert R Sabuncu. Hyperrecon: Regularization-agnostic cs-mri reconstruction with hypernetworks. In *International Workshop on Machine Learning for Medical Image Reconstruction*, pages 3–13. Springer, 2021. [3](#)
- [68] Chris Zhang, Mengye Ren, and Raquel Urtasun. Graph hypernetworks for neural architecture search. *arXiv preprint arXiv:1810.05749*, 2018. [3](#)
- [69] Xiangrong Zhang, Wenkang Ma, Chen Li, Jie Wu, Xu Tang, and Licheng Jiao. Fully convolutional network-based ensemble method for road extraction from aerial images. *IEEE Geoscience and Remote Sensing Letters*, 17(10):1777–1781, 2019. [2](#), [3](#)
- [70] Zhengxin Zhang, Qingjie Liu, and Yunhong Wang. Road extraction by deep residual u-net. *IEEE Geoscience and Remote Sensing Letters*, 15(5):749–753, 2018. [5](#)
- [71] Zhi-Hua Zhou. Ensemble learning. In *Machine Learning*, pages 181–210. Springer, 2021. [2](#), [3](#), [8](#)

	Conf. 1.	Conf. 2.	Conf. 3.	Conf. 4.	Conf. 5.	Conf. 6.	Conf. 7.	Conf. 8. (Ours)	Conf. 9. (Ours)	Conf. 10. (Ours)
Network Architecture	ResUNet	ResUNet	UNETR	ResUNet	UNETR	ResUNet	UNETR	ResUNet	UNETR	Hyper-ResUNet
Loss	Dice	Dice CE	Dice CE	Varying Tversky	Varying Tversky	Varying Tversky				
Drop-Out	None	None	None	0.1	0.1	0.1	0.1	None	None	None
No. Networks	1	1	1	1	1	5	5	5	5	1
No. Trainable Params	4.8M	4.8M	92.7M	4.8M	92.7M	4.8M (x5)	92.7M (x5)	4.8M (x5)	92.7M (x5)	130M
No. Epochs	2,000	2,000	2,000	2,000	2,000	2,000	2,000	2,000	2,000	3,000
Minibatch Size	8	8	8	8	8	8	8	8	8	8
Pre-Ensemble Setting	N/A	N/A	N/A	N/A	N/A	Data subsets/ Random Init	Data subsets/ Random Init	Random Init	Random Init	N/A
Ensemble Strategy	N/A	N/A	N/A	N/A	N/A	Average Ensemble	Average Ensemble	Average Ensemble	Average Ensemble	Average Ensemble

Table S. 1. The details of network architectures and training configurations of the comparison and proposed methods.

A. Network Architectures and Training Details

Network Architecture and Optimization Table S. 1 summarizes the network architecture and training details of the comparison and proposed methods. The number of epochs of the proposed hypernetwork architecture (Hyper-ResUNet) was set to 3,000 because the learning rate of the Adam optimizer was set to $1e^{-5}$ compared to the other methods with 2,000 epochs and $1e^{-4}$ learning rate. The kernel depths of the segmentation networks of all ResUNet-based configurations except the Hyper-ResUNet were 16, 32, 64, 128, and 256 for the five layers of encoders and decoders. The kernel depths of the Hyper-ResUNet was set to 32, 32, 64, 64, and 128. For the UNETR architecture, the sizes of the input patch, embedding, multilayer perceptron (MLP) sublayers were set to 16, 768, and 3,072, respectively, following their original implementation. The number of heads of the UNETR was set to 12.

Data Augmentation The same basic data augmentation strategies were applied to all configurations. The intensity range of each image \mathbf{I} was scaled to $[0, 1]$. For training, we randomly adjusted the contrast of images at each minibatch with random $\gamma \in \mathcal{U}(0.5, 4.5)$,

$$\mathbf{I}_{r.contr.} = (\mathbf{I} - \min(\mathbf{I}))^\gamma (\max(\mathbf{I}) - \min(\mathbf{I}) + \min(\mathbf{I})). \quad (\text{A.1})$$

Images and human annotation maps were randomly flipped by x-axis with 0.1 probability. Images and human annotation maps were randomly cropped to 192x192x16 patches which showed empirically best results for all configurations compared to 64x64x8 and 256x256x32 (e.g., full images). For inference, the intensity range of an input image was scaled to $[0, 1]$. At the inference stage, the input image was cropped sequentially to 192x192x16 patches and inferred by the sliding window technique with 80% overlap.

B. Segmentation Uncertainty Estimation

We can directly compute a segmentation uncertainty map from a segmentation probability map by the entropy,

$$H(\mathbf{y}) = - \sum_{i=1}^{N_L} (p(\mathbf{y}_i) + \epsilon) \log(p(\mathbf{y}_i) + \epsilon), \quad (\text{B.1})$$

where N_L is the number of labels (e.g., two for binary segmentation), $p(\mathbf{y}_i)$ is the probability of the label to be the i^{th} label (e.g., $\mathbf{y}_1 = 0$ and $\mathbf{y}_2 = 1$ for binary segmentation). ϵ is a small number for numerical stability. For binary segmentation, $H(\mathbf{y})$ is in the range of approximately (0.0, 0.7).

Figure S. 1 shows the examples of the estimated uncertainty maps. We set $\epsilon = 5e^{-5}$. The input images and human annotations were shown in Figure S. 1 (a) and (b), respectively. The uncertainty maps from the vanilla ResUNet with the Dice CE loss, the single UNETR with the drop-out rate of 0.1, and the UNETR ensemble with the 5-fold data subsets and random initialization are shown in Figure S. 1 (c-e), respectively. Those from the proposed the UNETR ensemble with the varying Tversky loss and the Hyper-ResUNet are shown in Figure S. 1 (f) and (g), respectively. The top two rows show the same examples with Figure 2. The areas that are ambiguous between acute stroke lesions, white matter hyperintensities, and possible image artifacts showed the high uncertainty. The same ambiguous areas showed the segmentation probability close to 0.5 in Figure 2. The bottom row of Figure S. 1 shows the example with the low ambiguity. The proposed methods (Figure S. 1 (f) and (g)) only captured the ambiguous area caused by lesion diffusion. It showed the proposed methods did not impose undesired additional uncertainty.

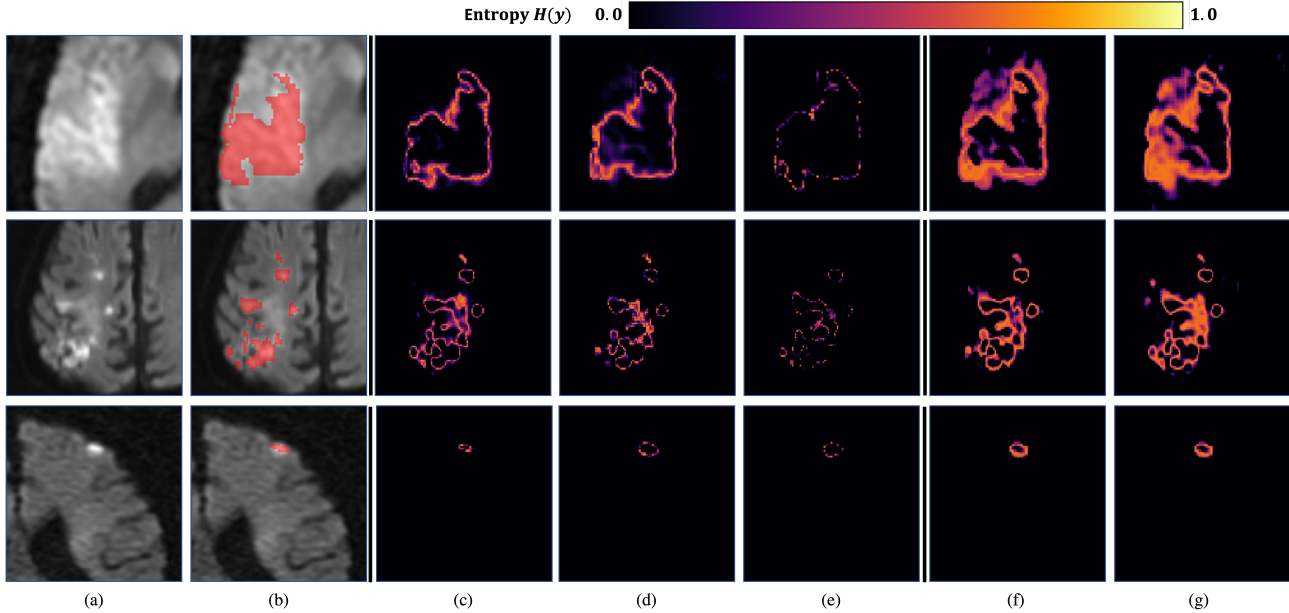


Figure S. 1. Examples of the estimated segmentation uncertainty maps. Zoomed and cropped input images and human annotations are shown in (a) and (b), respectively. (c-g) show the The uncertainty maps computed based on the segmentation probability maps. (c) The vanilla ResUNet, (d) UNETR with the drop-out rate of 0.1, (e) UNTER ensemble with 5-fold data subsets and random initialization, (f) our proposed UNETR ensemble with the varying Tversky loss, and (g) Hyper-ResUNet with the varying Tversky loss.

Hyper-vector Size	No. Mapping Layers	Primary Net Kernel Depths	Total No. Params	Training Time (GPU Hours)
None	None	[32,32,64,64,128]	6.0M	x
8	2	[32,32,64,64,128]	18.1M	19.4
16	3	[32,32,64,64,128]	34.1M	19.4
32	4	[32,32,64,64,128]	66.2M	19.8
64	5	[32,32,64,64,128]	130M	20.1
128	6	[32,32,64,64,128]	258M	21.5

Table S. 2. The configurations of the hypernetworks with different mapping network sizes.

C. Mapping Network

We investigate the effect of the different sizes of mapping networks and the mapped hypervectors in this section. The detailed configurations are summarized in Table S. 2. We fixed the configuration of the primary ResUNet to five-layer encoder and decoder with the kernel depths [32, 32, 64, 64, 128]. All hypernetworks were trained on NVIDIA Titan Xp (12GB GPU memory) with the batch size of 16 and 4,000 epochs. Figure S. 2 shows the Dice scores of the segmentation label maps estimated by the hypernetworks with different segmentation probability thresholds. The hypernetwork without the mapping network showed substantial decrease of the performance, 0.475 peak Dice score, and was not included in the plot.

We observed that the hypernetworks with larger mapping networks showed better Dice scores. However, the change

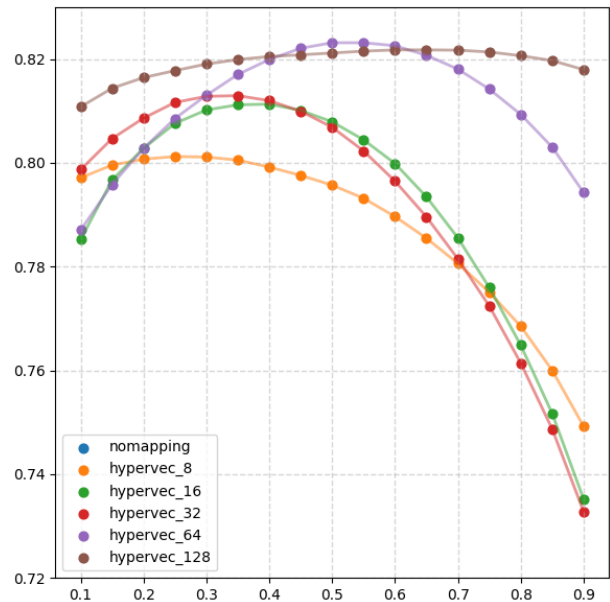


Figure S. 2. Dice scores with varying probability thresholds estimated by the hypernetworks with different mapping network sizes.

of the Dice scores with different segmentation probability thresholds decreased with the larger mapping network. We speculate that the hypernetwork might be overfit to data and human annotations when the size of the network increases. The performance improvement was also gradually saturated that the hypernetworks with the 4-layered and 5-layered

mapping networks showed similar highest Dice scores.

D. Primary Network

Conf.	Hypervector/ Mapping Layers	Primary Net Kernel Depths	Total No. Params	Training Time (GPU Hours)
P. 1.	32/4	[32,64,128,256,512]	634M	30.4*
P. 2.	32/4	[16,32,64,128,256]	158M	19.1
P. 3.	32/4	[32,32,64,64,128]	66.2M	19.7
P. 4.	32/4	[8,16,32,64,128]	39.7M	16.9
P. 5.	32/4	[16,16,32,32,64]	16.6M	17.0

Table S. 3. The configurations of the hypernetworks with different primary network sizes. All hypernetworks except Conf. P. 1. was trained on NVIDIA Titan Xp. (*) Conf P. 1. was trained on NVIDIA QRTX 5000.

formance change with respect to different primary network sizes was not consistent: i.e., the larger primary network size did not always result in better performance although Conf. P. 1. with the largest primary network size showed the best performance. However, we observed the decrease of the change of Dice scores over different segmentation probability thresholds similar to the hypernetworks with the larger mapping networks. We speculate that a hypernetwork tends to overfit when an overall size increases while the effect of the mapping network may be greater.

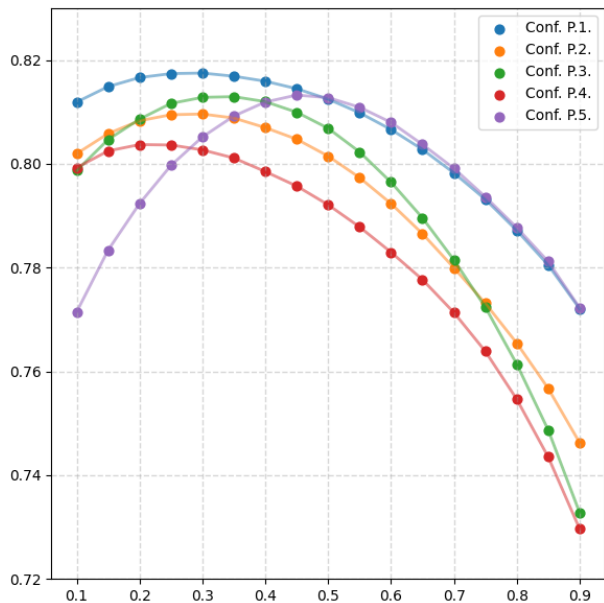


Figure S. 3. Dice scores with varying probability thresholds estimated by the hypernetworks with different primary network sizes.

We analyze the effect of the size of the primary segmentation network (ResUNet) on the hypernetwork performance in this section. Table. S. 3 summarizes the configurations of the hypernetworks with different primary network sizes. We fixed the hypervector size to 32 and the number of layers of the mapping network to four. We fixed the batch size to 16 and the maximum epochs to 4,000. The hypernetworks were optimized by the Adam optimizer with the $1e^{-5}$ learning rate and $1e^{-3}$ weight decay. Conf. P. 1. was trained on NVIDIA QRTX 5000 (16GB GPU memory) because of the large network size. The other configurations were trained on NVIDIA Titan Xp (12GB GPU memory). Figure. S. 3 shows the Dice scores of the hypernetworks with different primary network sizes. The per-